Effect of partial drainage on cyclic strengths of saturated sands in dynamic centrifuge tests

Kathleen M. Darby, S.M.ASCE (Corresponding author)
Senior Staff Engineer, Geosyntec Consultants, Oakland, CA 94607. E-mail: KDarby@Geosyntec.com

Ross W. Boulanger, F.ASCE
Professor, Department of Civil and Environmental Engineering, University of California at Davis, Davis, CA 95616. E-mail: rwboulanger@ucdavis.edu

Jason T. DeJong, M.ASCE
Professor, Department of Civil and Environmental Engineering, University of California at Davis, Davis, CA 95616. E-mail: jdejong@ucdavis.edu

Authors' final copy (Jan 2019) prior to copyediting and
publication by JGGE

ABSTRACT

The effects of partial drainage on the cyclic strength of saturated sand in a set of dynamic centrifuge model tests were evaluated. Three models of level profiles of saturated Ottawa F-65 sand with initial relative densities of 25, 43, and 80% were tested using a 9-m radius centrifuge. Models were subjected to multiple sinusoidal shaking events with acceleration amplitudes ranging from 0.03 to 0.55*g*. The cyclic resistance ratios (*CRR*) obtained from inverse analyses of dense accelerometer and pore pressure transducer arrays were correlated with cone penetration resistances (q_{c1N}) from in-flight cone penetration tests. Time histories of volumetric strain and surface settlement due to partial drainage were determined by inverse analyses of the array data and compared with measured surface settlements. The effect of volumetric strain on cyclic strength is examined through single element simulations using the constitutive model PM4Sand (version 3). Results of these simulations are compared to prior laboratory and numerical studies investigating the effect of partial saturation on cyclic strength. The magnitude of the volumetric strains developed in the centrifuge models due to partial drainage and their effects on the centrifuge *CRR*-q_{c1N} correlation are examined.

INTRODUCTION

The response of a potentially liquefiable soil deposit during seismic loading can be strongly affected by the extent and degree to which excess pore water pressures diffuse during and after strong shaking. The degree of partial drainage during earthquake shaking for thick layers of sandy soils (e.g., sands, silty sands, sandy silts) subjected to shorter duration motions is usually assumed small enough that fully undrained conditions apply. The degree of partial drainage can increase as the boundaries become more pervious, liquefiable layer thickness decreases, hydraulic conductivities increase, compressibility decreases, and shaking duration increases. Partial drainage during and after strong shaking can be enhanced by installation of drainage elements, which can increase resistance to liquefaction triggering and reduce the deformations that develop after liquefaction triggering (e.g., Howell et al. 2012). The potential effects of partial drainage have been recognized for decades (e.g., NRC 1985, Whitman 1985), particularly with regards to void redistribution in interlayered soils or sloping ground (e.g., Kokusho 2003, Kulasingam et al. 2004, Malvick et al. 2006, 2008), but remain challenging to quantify for individual case histories or centrifuge model studies.

Centrifuge tests have been used to gain insight into the effects of pore pressure diffusion on liquefaction behaviors through the use of dense sensor arrays within models. Kulasingam et al. (2004) performed a set of 1-m radius centrifuge tests to investigate the influence of site geometry (e.g. slope angle, relative density, permeability contrast) and ground motion (e.g. duration, shaking history) on shear strain localization. Kutter et al. (2008) used dense arrays of pore pressure transducers (PPTs) around a tunnel embedded in liquefiable soil to investigate the mechanisms governing uplift of the tunnel during earthquake shaking. Malvick et al. (2006, 2008) and Kamai et al. (2010) used inverse analysis techniques to compute profiles of volumetric strain from densely

spaced PPT arrays in centrifuge models designed to investigate void redistribution in sand layers with embedded low-permeability silt layers or overlying low-permeability clay layers.

A number of researchers have examined the relationship between degree of saturation and cyclic strength and generally observed an increase in cyclic strength as the degree of saturation decreases (e.g. Yoshimi et al. 1989, Okamura and Soga 2006). Okamura and Soga (2006) demonstrated a unique relationship between the volumetric strain that develops during the loading of unsaturated soil and the cyclic resistance ratio. Okamura et al. (2018) further examined the relationship for saturated sands by using triaxial and centrifuge tests to induce volumetric strain with non-liquefaction pre-shearing events. The relationship between pre-shearing induced volumetric strain and liquefaction resistance was found to be consistent with the relationship for unsaturated soils (Okamura et al. 2018).

The present study evaluates the effect of partial drainage on the cyclic resistance ratio (*CRR*) of saturated sand and its correlation to cone penetration tip resistance (q_c) in a series of dynamic centrifuge model tests. Inverse analysis techniques examine the evolution of volumetric strains due to partial drainage in a set of three saturated, clean sand centrifuge models subjected to multiple shaking events. The three models had an upper layer of Ottawa F-65 sand that was placed loose for two models (initial relative density (D_{Ro}) of 43% and 25%) and dense for one model (D_{Ro} of 80%). Densely spaced PPTs provide time histories of pore pressure with depth. Inverse analyses of the PPT data provide profiles of volumetric strain and settlement in time. Volumetric strain and partial drainage behaviors in representative shaking events are presented in detail to illustrate their relation to system-level dynamic behaviors. The potential effects of these volumetric strains on the *CRR*-q_c relationship, as derived in previous work (Darby et al. 2018b), are investigated with single element simulations using the PM4Sand constitutive model in FLAC. These analyses are

compared to previous laboratory and constitutive modeling studies examining the effect of volumetric strains due to partial saturation on cyclic strength. Results of these analyses are used to re-examine the *CRR* values derived from previous inverse analyses of these centrifuge data, and subsequently adjust the *CRR*-q_c correlation for partial drainage effects.

CENTRIFUGE MODELS

A set of three centrifuge models were constructed in a flexible shear beam container and tested at the UC Davis Center for Geotechnical Modeling. These tests are described in Darby et al. (2018b), and thus only briefly described herein. Models consisted of an approximately 245-273 mm (model scale) thick layer of Ottawa F-65 sand overlying an 180 mm thick layer of Monterey sand and a 40 mm thick gravel saturation base layer, as shown in Figure 1. Ottawa sand was placed by dry pluviation at D_{Ro} of 43%, 25%, and 80%, in each of the three models, respectively. Monterey sand was placed by dry pluviation at D_{Ro} of 85% in all models. Closely spaced vertical arrays of PPTs and accelerometers (ACC) were placed at matching depths throughout the Ottawa sand layer to capture pore pressure generation/dissipation and accelerations throughout the profile; sensors were placed at greater vertical spacing throughout the Monterey sand layer. Sensor locations are provided in the representative cross-section shown in Figure 1. Four linear potentiometers (LP) measured surface settlement. Models were saturated under vacuum with a viscous pore fluid prepared to 0.00002 m^2/s (model scale) and tested at a centrifuge acceleration of 40g. Results are presented in prototype dimensions based on standard scaling relations for dynamics, unless otherwise noted.

Each model was subjected to a series of shaking events with progressively increasing amplitudes of acceleration. Model 1 was subjected to 29 shaking events, Model 2 was subjected to 26 shaking events, and Model 3 was subjected to 17 shaking events. Each shaking event

consisted of 15 cycles of a 1 Hz frequency uniform sine wave with amplitudes of acceleration ranging from 0.03 to 0.55 *g*. The testing sequence and select responses for Model 1 are presented in Figure 2; the testing sequences for the other two models were similar. Points are plotted against the peak base acceleration (PBA) for each shaking event. The excess pore pressure ratio ($r_u = u_e/\sigma'_{vo}$) is shown for three depths in the Ottawa sand layer: circles represent one-third depth, diamonds represent mid-depth, and triangles represent two-thirds depth. The color of the points indicates the maximum r_u generated during each event, with red points having high r_u ($r_u \geq 0.95$), open points having low r_u ($r_u < 0.70$), and yellow points having intermediate r_u ($0.70 \leq r_u < 0.95$). In-flight cone penetration tests were performed before or after select events in each model to capture progressive changes in penetration resistance resulting from the multiple shaking events. Timing of the cone penetration tests are indicated by the blue arrows across the top x-axis in Figure 2. The cone penetration resistance reported at times in between when the cone penetration tests were performed was assumed to vary linearly with the measured ground surface settlements; this linear interpolation was used to obtain cone penetration resistances prior to all shaking events not immediately preceded by an in-flight cone penetration test.

Cyclic stress ratios (*CSR*s) were calculated using inverse analysis of accelerometer array data and paired with overburden corrected, normalized cone penetration resistances ($q_{c1N} = C_N q_c/P_a$, where P_a = atmospheric pressure, C_N = overburden correction factor) at corresponding depths for every shaking event in each of the three models. Irregular *CSR* time series were extracted at elevations midway between PPTs and converted to equivalent uniform *CSR* time series using the fatigue based cycle weighting procedure described in Seed et al. (1975). For shaking events triggering $r_u \geq 0.95$, equivalent uniform CSR_{15cyc} were calculated only considering loading prior to triggering, making these CRR_{15cyc}. CSR_{15cyc} and CRR_{15cyc} were then adjusted to a common

overburden stress and reduced to account for bi-directional shaking to facilitate comparisons to case history based correlations. Additional details on the calculation of $CRR_{15cyc,\sigma'=1}$ from *CSR* time series are provided in Darby et al. (2018b). $CRR_{15cyc,\sigma'=1}$ were paired with corresponding q_{c1N} values and classified as either high, medium, or low confidence based on their sensitivity to various sources of experimental uncertainty. A high confidence classification was assigned to $CRR_{15cyc,\sigma'=1}$ values for which uncertainty in liquefaction triggering time and behavior due to sensor location changed the $CRR_{15cyc,\sigma'=1}$ by less than 20%. A low confidence classification was assigned to $CRR_{15cyc,\sigma'=1}$ values where these uncertainties changed the $CRR_{15cyc,\sigma'=1}$ by greater than 20%. A medium confidence classification was assigned to $CRR_{15cyc,\sigma'=1}$ that met all the criteria for high confidence with the exception that PPTs above and below the location $CRR_{15cyc,\sigma'=1}$ were extracted did not both indicate $r_u \geq 0.95$. Additional details on the classification of the *CRR*-q_{c1N} pairs can be found in Darby et al. (2018b). In general, centrifuge *CRR*-q_{c1N} pairs show good agreement with case history based liquefaction triggering correlations within the range for which the correlations are constrained. However, a number of the *CRR*-q_{c1N} pairs fall above or slightly below the case history correlations. This study examines the potential influence of partial drainage on the centrifuge *CRR*-q_{c1N} relationship and their comparison to case history based correlations.

CALCULATION OF VOLUMETRIC STRAINS IN CENTRIFUGE TESTS FROM PPTS

Profiles of volumetric strain were computed from PPT data following the procedure in Malvick et al. (2008) with the numerical smoothing function modified to account for the different boundary conditions and better fit the experimental data. Hydraulic gradient (i) and volumetric strain rate ($\frac{\partial \varepsilon_v}{\partial t}$) are related to excess pore pressure (u_e) as:

$$i = \frac{\partial(\Delta u)}{\partial z}\frac{1}{\gamma_w} \tag{1}$$

$$\frac{\partial \varepsilon_v}{\partial t} = -\frac{k_v}{\gamma_w}\frac{\partial^2(u_e)}{\partial z^2} \tag{2}$$

where k_v is the vertical permeability of the soil and γ_w is the unit weight of water. The prototype k_v was taken as 0.033 cm/s for Ottawa sand (data from Parra Bastidas et al. 2016) and 0.4 cm/s for Monterey sand (data from Kutter et al. 2008) based on the permeability measured with pure water times the model scale factor (40) and divided by the pore fluid viscosity scale factor (20). Some researchers have observed permeability to evolve during liquefaction (e.g. Arulanandan and Sybico (1992), Jafarzadeh and Yanagisawa (1995), Balakrishnan (2000), Taiebat et al. (2007)); in this study permeability is held constant prior to and during liquefaction. The use of a constant permeability after the initiation of liquefaction suggests volumetric strains computed after liquefaction will underestimate reality. However, since the focus of this study is on the influence of volumetric strain prior to liquefaction, the constant permeability simplification is considered reasonable. Profiles of volumetric strain were determined by integrating the volumetric strain rate computed in equation (2) with respect to time. Numerical smoothing of measured PPT data with respect to depth using a least-squares curve fitting procedure eliminated the high-frequency noise that can develop during differentiation of discrete data and enabled the direct differentiation and integration calculations described in equation (2). The curve fitting procedure used the functional form:

$$u_e(z) = a_0 z^6 + a_1 z^5 + a_2 z^4 + a_3 z^3 + a_4 z^2 + a_5 z \tag{3}$$

The above functional form satisfies the boundary condition of zero excess pore pressure at the surface, and provided a better fit to the pore pressure profiles in these layered models compared to the functional form used by Malvick et al. (2008) for a uniform sand profile with an embedded silt layer. Smoothing was performed for each time step (0.008 seconds) from the start of shaking to 200 seconds after shaking ended (sufficient for full dissipation of excess pore pressures) for all shaking events (72 events total). Analyses using alternative functional forms for this smoothing process provided similar volumetric strains for most cases and did not significantly affect the overall trends or conclusions presented later.

Representative profiles of excess pore pressure and volumetric strain are presented in Figure 3 for the tenth shaking event in Model 1 (PBA of 0.12g). The tenth shaking event in Model 1 is presented to illustrate typical behaviors observed in the majority of shaking events in all three models. Pore pressure isochrones from numerical smoothing and measured data are shown for select times after the end of shaking in the far left panel. Also shown are the computed profiles of volumetric strain (ε_v) at the end of shaking (solid red curves) and at the end of dissipation (dashed purple curves). For reference, the locations of ACCs and PPTs in the Ottawa sand layer are shown in the far right panel of Figure 3. As shown in Figure 3, the majority of volumetric strain develops during dissipation after the end of shaking. During dissipation, positive (contractive) volumetric strains develop throughout the entire Ottawa sand layer, exceeding 1% in the upper 2 m. The behavior shown in Figure 3 is representative of behavior observed later in the shaking sequence (after approximately 10 shaking events) in the initially loose models (Models 1 and 2), and during all events in the initially dense model (Model 3). Early in the shaking sequence of the initially loose models, negative volumetric strains (dilation or loosening) tend to develop in the upper 2 m, while the remainder of the profile develops contractive volumetric strains. Note that the

development of positive (contractive) and negative (dilative) volumetric strains caused by reversed-cyclic loading coupled with complex pore pressure diffusion patterns are not comparable to the volumetric strains that would be expected in monotonic drained loading of similar relative density sands. The responses from shaking event 2 in Model 1 (the first event to trigger liquefaction for this model) and shaking event 10 in Model 2 (an initially looser model with the same shaking history as for Model 1) are shown in Darby et al. (2018a).

Profiles of CSR and estimated penetration resistances measured in the Ottawa sand layer for the tenth shaking event in Model 1 are also shown in Figure 3. The *CSR*s shown are the equivalent uniform CSR_{15cyc} for the entire shaking event calculated using the procedures summarized previously and described in detail in Darby et al. (2018b). As shown, CSR_{15cyc} values are largest in the upper 2 m, and decrease and become more uniform below 3 m depth. Profiles of q_{c1N} are shown before shaking (solid black curve) and after shaking (dashed purple curve). These profiles are interpolated from the measured penetration resistances (obtained after six and twelve shaking events) using the procedure described previously. Examination of the cone profiles in Figure 3 indicates a minimal change in penetration resistance after a single shaking event.

Time series of hydraulic gradient, volumetric strain rate, and volumetric strain at 2 m, 4 m, and 6 m depth in the Ottawa sand layer for the tenth shaking event in Model 1 (the same event shown in Figure 3) are shown in Figure 4a-c. Gradients are plotted in the top row, volumetric strain rates are plotted in the middle row, and volumetric strains are plotted in the bottom row. Data are shown from the start of shaking through 250 seconds after the start of shaking. Grey shading indicates the duration of shaking in all plots. In the plots of gradient, data are shown for a 0.2 m interval across the labeled depth; i.e., blue curves correspond to depths of 1.9 m, 3.9 m, and 5.9 m, while red curves correspond to depths of 2.1 m, 4.1 m, and 6.1 m. The graphs for

volumetric strain rate and volumetric strain are for the labeled depth only. Examination of the gradients around these three depths illustrate different features of the diffusion process. At 2 m depth, gradients reach peak values slightly greater than unity, while gradients at 4 m and 6 m reach values never exceeding 0.8; these gradients correspond to the measured PPT data shown in Figure 3, indicating liquefaction (in terms of $r_u \approx 1$) only occurs in the upper portion of the Ottawa sand. The gradients at 2.1 m, 4.1 m and 6.1 m depths are smaller than the gradients at 1.9 m, 3.9 m and 5.9 m depths, respectively (except briefly at 2 m depth from approximately 9 to 13 seconds when the gradients are nearly identical), which indicates a net outflow of pore water into these 0.2-m-thick depth intervals. The corresponding volumetric strain rates at 2 m, 4 m and 6 m depths are therefore always positive, and the integrated volumetric strains are similarly always positive. The integrated volumetric strain at 2 m depth levels off at a value of approximately 0.1% during the four second time period when there are similar gradients at 1.9 m and 2.1 m, after which it progressively increases toward its final value of about 1% after full dissipation. The volumetric strain rates correspond to the curvature of the pore pressure isochrones in Figure 3, which consistently indicate net outflows near the middle of the model. The time histories of volumetric strain at these three depths support the observation in Figure 3 that the majority of volumetric strain is generated during pore pressure dissipation.

Partial drainage and dynamic responses

Time histories of volumetric strains, hydraulic gradients, and surfaces settlements from the inverse analyses provide insights into the dynamic and post-dynamic responses of the Ottawa sand layer. For example, detailed responses near the middle of the Ottawa sand layer are shown in Figure 5 for the tenth shaking event (PBA of 0.12*g*) for Model 1. Time histories during and after strong shaking are shown in the two right panels, whereas excess pore pressure isochrones and sensor

locations are shown in the two left panels. Note the time scale on the x-axis changes between the panel for during shaking and the panel for after shaking. Time histories of surface settlement are plotted in the top graphs; the computed settlements (green lines) are smaller than those measured by LPs during shaking (grey lines), but fall within the range measured by LPs during dissipation. Time series for r_u, i, ε_v and acceleration are shown for the 5.0-6.0 m depth interval; i.e., the grey shaded interval in the isochrones panel, where the orange star indicates the depth, z^*, at which volumetric strain is computed (5.5 m). This shaded region was selected to investigate volumetric strain behavior between PPTs with different triggering responses. The r_u reached 1.0 at the PPT above z^* (blue line) but did not exceed about 0.8 below z^* (red line). The hydraulic gradients above z^* (blue line) is greater than below z^* (red line) for the first 75 seconds, indicating a net out-flow of pore water from this depth interval during this time. In fact, the results during the time interval of 5-12 seconds after the start of shaking show the gradient above z^* is positive (indicating upward flow) while the gradient below z^* is negative (indicating downward flow). Approximately 75 seconds after the start of shaking the gradients above and below z^* converge, indicating almost zero net flow from this depth interval. Volumetric strain at z^* indicates slight volumetric contraction during shaking (about 0.1%), increasing to a final volumetric contraction of about 0.32% after dissipation. The accelerations below z^* (red line) show minimal amplification and phase-shift relative to the base acceleration (black line), consistent with liquefaction not being triggered at or below this depth. The accelerations above z^* (red line) show high-frequency spikes and visible phase-shifts relative to the base acceleration starting approximately 10 seconds into shaking, which is consistent with the generation of $r_u = 1.0$ at this depth and time.

Volumetric strains prior to triggering of liquefaction

Time series of volumetric strain are used to determine the strains that developed during the entire shaking sequence and prior to the triggering of r_u = 1.0 (i.e., $\varepsilon_{v,t}$) at the three depth intervals at which *CRR*-q_{c1N} pairs were computed; these volumetric strains are shown in Figure 6 a-c. Figures 6a and 6b compare the volumetric strains developed during the entire shaking sequence to the equivalent uniform $CSR_{15cyc,\sigma'=1}$ for non-triggering and triggering events, respectively. Volumetric strains developed during the full shaking sequence range from -0.056% to 0.099% for non-triggering points and from -0.23% to 0.28% for triggering points. Figure 6c compares the volumetric strains developed prior to triggering to the $CRR_{15cyc,\sigma'=1}$ for triggering events only. The color and shape of the points in Figure 6c indicate the *CRR* confidence, described previously and in more detail in Darby et al. (2018b). Volumetric strains developed prior to triggering range from -0.1% to 0.15% for all three depth intervals and centrifuge models, with the majority of the high confidence *CRR* points having negative volumetric strain prior to triggering being from the shallower depths. These volumetric strains are of particular interest because they would contribute to potential increases or decreases in the liquefaction resistance of the soil at any given depth. Figure 6 suggests a greater tendency overall to develop positive volumetric strains than negative volumetric strains, and that for *CSR* or *CRR* values less than approximately 1.0, the amount of volumetric strain generated does not appear biased by the cyclic stress applied to the soil; at *CSR* or *CRR* values greater than approximately 1.0, volumetric strains appear biased toward being dilative. Comparison of Figure 6b and c indicates that volumetric strain continues to develop after

the triggering of $r_u = 1.0$. Additional detail on events generating negative volumetric strain is provided in Darby et al. (2018a).

Volumetric strains for each of the *CRR*-q_{c1N} pairs are shown in Figure 7, binned by $CRR_{15cyc,\sigma'=1}$ confidence, with the shading of the point indicating $\varepsilon_{v,t}$ for triggering points and $\varepsilon_{v,nt}$ for non-triggering points. Dilative volumetric strains are shown in red, whereas contractive volumetric strains are shown in blue; darker shades correspond to larger absolute values of volumetric strain and lighter shades correspond to smaller absolute values of volumetric strain. These are the same points that were shown previously in Figures 6a and 6c, but are now plotted against q_{c1N}. Note that the y-axes in Figure 7 plots extend from $CRR_{15cyc,\sigma'=1}$ values of 0 to 1.0 and the x-axes in Figure 7 plots extend from q_{c1N} values of 0 to 350; while this study produced data outside these axes limits, these data were not shown for the sake of figure legibility. Trends in the data outside the shown limits are generally consistent with the trends shown in Figure 7. Also shown in Figure 7 plots are the Boulanger and Idriss (2015) case history based liquefaction triggering correlations for 16, 50, and 84% probability of liquefaction, only considering model uncertainty. Volumetric strains for triggering pairs range from -0.99% to 0.15%; volumetric strains for non-triggering pairs range from -0.056% to 0.099%. Of the 20 high confidence *CRR*-q_{c1N} pairs, eight have dilative $\varepsilon_{v,t}$ of 0.004% to 0.099% and 17 have contractive $\varepsilon_{v,t}$ of 0.008% to 0.081%. Of the eight medium confidence *CRR*-q_{c1N} pairs, one has dilative volumetric strain of 0.009%, and seven have contractive $\varepsilon_{v,t}$ of 0.003% to 0.051%. Of the 67 low confidence *CRR*-q_{c1N} pairs, ten have dilative $\varepsilon_{v,t}$ of 0.005% to 0.067% and 57 have contractive $\varepsilon_{v,t}$ of 0.001% to0.15%. Of the 120 non-triggering *CSR*-q_{c1N} pairs, 26 have dilative $\varepsilon_{v,t}$ of 0% to 0.056% and 84 have contractive $\varepsilon_{v,t}$ of 0% to 0.099%. The *CRR*-q_{c1N} pairs with dilative $\varepsilon_{v,t}$ would be expected to have had greater *CRR*s if the soil had been perfectly undrained (i.e., no volume change), whereas

the *CRR*-q_{c1N} pairs with contractive $\varepsilon_{v,t}$ would have had smaller *CRR*s if the soil had been perfectly undrained.

EFFECT OF PARTIAL DRAINAGE ON CRR

The effect of partial drainage on *CRR* is investigated with single element simulations of undrained direct simple shear (DSS) loading using the constitutive model PM4Sand (version 3) in the finite-difference code FLAC (version 8) (Itasca (2016)). PM4Sand is a stress-ratio controlled, critical state based, bounding surface plasticity model developed for earthquake engineering applications (Ziotopoulou and Boulanger 2016, Boulanger and Ziotopoulou 2017). The PM4Sand model was calibrated for Ottawa sand following the procedure outlined in Boulanger et al. (2017) in which the primary parameters (D_R, shear modulus coefficient G_o, contraction rate parameter h_{po}) and the secondary parameters (maximum void ratio e_{max}, minimum void ratio e_{min}) are based on data by Parra Bastidas (2016) and Alarcon-Guzman et al. (1989); default values are used for the remaining secondary parameters. Analyses are performed for three D_R (35, 63, and 80%) and four levels of initial vertical effective stress (0.35, 0.50, 0.63, and 1.0 atm). *CRR*s are defined using two failure criteria: (1) 3% single amplitude shear strain (γ) in 15 cycles, and (2) r_u=0.98 in 15 cycles. The effect of both contractive (flow out of an element) and dilative (flow into an element) volumetric strains on *CRR* are examined.

Contractive volumetric strains that develop during cyclic loading due to net flow out of a saturated element are analogous to contractive volumetric strains that can develop due to compression of the pore fluid in a partially saturated element. Partially saturated elements experience compression of the air in the pore space in parallel with the generation of excess pore pressure during cyclic loading. A number of researchers have investigated the influence of partial saturation on cyclic strength using both experimental methods (e.g. Okamura and Soga 2006,

Yoshimi et al. 1989) and simulations (Zhang et al. 2016). Okamura and Soga (2006) performed a series of triaxial tests on Toyoura sand at D_R= 40%, with effective confining pressures of 0.19, 0.48, and 0.97 atm, and degrees of saturation ranging from 70-100%. Yoshimi et al. (1989) performed a set of cyclic torsional shear tests on hollow cylindrical Toyoura sand specimens at D_R=60% with effective confining pressures of 0.97 atm, and degrees of saturation ranging from 69-100%. Zhang et al. (2016) performed simulations of Toyoura and Nevada sand at D_R=30, 50, and 70%, effective confining pressures of 0.49 and 0.99 atm, and degrees of saturation ranging from 75-98% using a coupled hydromechanical elastoplastic constitutive model for unsaturated sands. Both Okamura and Soga (2006) and Yoshimi et al. (1989) used a 5% double amplitude shear strain criteria to determine *CRR*, while Zhang et al. (2016) used an excess pore pressure criteria of r_u=0.90 to determine *CRR*. The study by Okamura et al. (2018) showed the relationship between cyclic strength and volumetric strain due to drainage of saturated sands subjected to preshaking in centrifuge model tests is consistent with the effect of volumetric strain due to compression of pore fluid in laboratory tests on partially saturated sands with degrees of saturation ranging from 70-100%. The effects of matric suction are neglected in the comparison to the laboratory tests and simulations on unsaturated sands. Matric suction has been observed to increase soil stiffness which can influence settlement and volumetric strain (Ghayoomi et al. 2013, Morteza and Ghayoomi 2017). The implications of neglecting matric suction are discussed later. Despite these limitations, comparison of the partial drainage data to the partial saturation data can still provide insight into the influence of volumetric strain on *CRR*. Accordingly, the data from these studies of partial saturation can be used to (1) evaluate the numerical analysis methods used herein for investigating the effect on *CRR* of contractive volumetric strains due to net flow out during cyclic loading, and (2) provide confidence in the application of the numerical analysis

approach investigating the effect on *CRR* of dilative volumetric strains due to net flow in during cyclic loading, for which laboratory data are not available. *CRR*s defined using the shear strain criteria are used to compare the results of the single element simulations to laboratory data; *CRR*s defined using the excess pore pressure criteria are used to compare to the simulations by Zhang et al. (2016) and for the adjustment of the centrifuge *CRR*-q_{c1N} pairs.

Effect of contractive volumetric strains on *CRR*

Partial drainage during single-element simulations of cyclic DSS loading was modeled by two approaches: (1) by assuming volumetric strain is proportional to excess pore pressure, and (2) by imposing a volumetric strain rate proportional to the shear strain rate. In the first approach, a range of volumetric strains is produced by using a range of values for the bulk modulus of the pore fluid. In the second approach, a range of volumetric strains is produced by using different ratios of volumetric to shear strain rates (e.g., as used by Kamai and Boulanger 2012). Figure 8 compares dynamic responses from these two approaches using the γ=3% criteria for the D_R=63% simulation under conditions generating a volumetric strain of approximately 0.1% after 15 uniform loading cycles. The *CSR* required to trigger liquefaction in 15 cycles is 0.20 for purely undrained conditions, whereas it has increased to about 0.28 and 0.23 for the volumetric strain of 0.1% imposed using Approaches 1 and 2, respectively. The stress-strain and pore pressure responses for the two approaches show similar trends, although there are some notable differences. The first difference is in pore pressure behavior: while Approach 1 reaches r_u=1.0 sooner than Approach 2, Approach 2 starts building pore pressure earlier in loading. The second difference is in shear strain accumulation behavior: once shear strains reach 1%, Approach 1 requires three additional cycles to reach 5% shear strain, compared to Approach 2, which takes six additional cycles to reach 5% shear strain.

The effect of ε_v on $CRR_{\gamma=3\%,15cyc}$ from the two single element simulation approaches for modeling ε_v are shown in Figure 9 for all three D_R at a confining stress of 1.0 atm. CRR-ε_v pairs from Approach 1 are shown as circles with dashed trend lines; CRR-ε_v pairs from Approach 2 are shown as triangles with solid trend lines. The relative density is indicated by color, with blue, green, and red corresponding to a D_R of 35, 63, and 80%, respectively. As shown in Figure 9, increasing D_R shifts the curves upward without much shape change for ε_v below approximately 1.0% for both approaches. For all D_R at ε_v greater than approximately 0.01%, for a given ε_v, Approach 1 gives larger $CRR_{\gamma=3\%,15cyc}$ compared to Approach 2. However, trends from both approaches suggest contractive ε_v less than about 0.01-0.02% minimally effect $CRR_{\gamma=3\%,15cyc}$.

The effect of contractive ε_v on $CRR_{\gamma=3\%,15cyc}$ and $CRR_{ru=0.98,15cyc}$ from the single element simulations in this study are compared to the results of laboratory studies by Okamura and Soga (2006) and Yoshimi et al. (1989) and simulations by Zhang et al. (2016), in Figures 10a and 10b, respectively. Data shown in Figure 10 are all at a confining stress of approximately 1.0 atm. In Figures 10a and 10b data from this study are presented as circles and triangles for Approach 1 and 2, respectively, with D_R=35% indicated in blue and D_R=63% is indicated in green. Data from Okamura and Soga (2006) and Yoshimi et al. (1989) are shown in Figure 10a as orange and yellow squares, respectively, and correspond to Toyoura sand at D_R= 40, and 60%, respectively. Simulation data from Zhang et al. (2016) on Toyoura sand (D_R of 50 and 70%) and Nevada sand (D_R of 30 and 50%) are shown in Figure 10b as purple and tan diamonds, respectively. For both sands, darker shading corresponds to higher D_R and lighter shading corresponds to lower D_R. Volumetric strains from partial saturation data were computed using the method described in Okamura and Soga (2006). In general, these previous laboratory and simulation CRR_{15cyc}-ε_v pairs tend to fall within the D_R= 35-63% band from this study. The ε_v for the partial saturation laboratory

test data are generally larger than 0.30%, while the ε_v from Approach 2 in this study are smaller than 0.20-0.45% for D_R of 35% and 63%, respectively.

The change in cyclic strength due to volumetric strain is referred to as the liquefaction resistance ratio (*LRR* where $LRR=CRR_{\varepsilon v}/CRR_{\varepsilon v=0}$). Figure 11 shows the relationship between *LRR* and contractive ε_v for the simulations performed herein using the 3% shear strain failure criteria (Figure 11a) and laboratory data (Figure 11b). Also shown in Figure 11a are the results of the simulations for confining stresses of 0.35, 0.5, and 0.65 atm. As indicated in Figure 11a, in *LRR*-ε_v space, for a given approach, neither D_R nor confinement appears to significantly influence the results, with the primary exception being the data from Approach 1 at D_R=80% and $\varepsilon_v > 0.3\%$. Best fit curves for Approach 1 and Approach 2 are shown in cyan and magenta, respectively. The best fit curves for Approach 1 and Approach 2 for both failure criteria (γ=3% and r_u=0.98) are compared in Figure 11b to the *LRR*-ε_v relationship proposed by Okamura and Soga (2006) based on partial saturation data from literature. At $\varepsilon_v < 0.01\%$, all correlations indicate a minimal increase in *CRR,* with the exception of Approach 1 using the r_u=0.98 criteria. At ε_v between 0.01% and 0.20%, the correlations from Approach 1 using both failure criteria, and Approach 2 using the r_u=0.98 criteria, suggests a greater effect on *CRR* compared to the correlation from Okamura and Soga (2006), while the correlation from Approach 2 using the γ=3% criteria suggests a smaller effect on *CRR* compared to the correlation from Okamura and Soga (2006). At $\varepsilon_v > 0.20\%$, the correlation from Approach 2 using the γ=3% criteria suggests a large increase in *CRR* for increasing ε_v. While the curvature of the correlations from Approach 1 using the γ=3% criteria and Approach 2 using the r_u =0.98 criteria show greater agreement with the curvature of the correlation from Okamura and Soga (2006), at ε_v <0.30% the amount of increase in *CRR* from

Approach 2 using the γ=3% criteria is more consistent with the increase in *CRR* from Okamura and Soga (2006).

The excess pore pressure, shear strain, and normalized volumetric strain generation patterns from single element simulations using the r_u=0.98 criteria are compared in Figure 12 to centrifuge test data for mid-depth during a shaking event producing comparable levels of cyclic loading. Also shown are the results of the single element simulations for purely undrained loading under a uniform *CSR* of 0.22. In Figure 12a results from Approach 1 and Approach 2 are shown as dotted purple lines and solid green lines, respectively; results for purely undrained conditions are shown as dashed orange lines. The undrained condition generates pore pressure and shear strain more rapidly than the partially drained condition. The simulations used a uniform *CSR* of 0.22 and developed volumetric strains of 0.008% and 0.012% after 13.5 uniform loading cycles for Approach 1 and Approach 2, respectively (Figure 12a). The centrifuge model has an irregular *CSR* time series, and develops a volumetric strain of 0.072% after about 10 shaking cycles (Figure 12b). For the centrifuge model, time series of r_u at the PPT above mid-depth is shown as a solid blue curve and from the PPT below mid-depth is shown as a dashed red curve. Comparing the shapes of the ε_v time series in the two simulation approaches and the centrifuge model suggest simulation Approach 2 is more representative of the behavior occurring in the centrifuge for this shaking event. Simulation Approach 2 and the centrifuge model develop ε_v at a relatively uniform rate, and continue to develop ε_v after triggering $r_u \approx 1.0$. In contrast, simulation Approach 1 produces a more rapid ε_v generation early in loading, and ceases ε_v generation once r_u=1.0. Based on the results shown in Figure 12, the *LRR*-ε_v trend from Approach 2 with the r_u=0.98 criteria will be used to adjust the centrifuge data to account for contractive ε_v.

Effect of dilative volumetric strains on CRR

Dilative volumetric strain in single element simulations was modeled by assuming the volumetric strain rate is proportional to the shear strain rate (Approach 2). Neither laboratory nor simulation data examining dilative ε_v are available, but the reasonable agreement between the single element simulations and experimental data on contractive ε_v suggest the approach described in this study is not unreasonable. The effect of dilative ε_v on *CRR* and *LRR* are shown in Figures 13a and 13b, respectively, for a confinement of 1 atm, and D_R of 35, 63, and 80% using the γ=3% criteria. Figure 13c compares the best fit curves from the single element simulations using the γ=3% and r_u=0.98 criteria. Figure 13a indicates a reduction in *CRR* with increased dilative ε_v, with similar trends for all three D_R. This reduction in *CRR* with increased dilative ε_v for all D_R is also shown in Figure 13b, along with results for D_R=63% at confinements of 0.35, 0.50, and 0.65 atm, suggesting relatively little dependence on D_R or confinement. This observation is consistent with the observations for contractive ε_v, though it is worth noting that the effect of dilative ε_v on *CRR* does have a slightly greater dependence on D_R compared to the effect of contractive ε_v on *CRR*. Dilative ε_v below 0.01% minimally decreases *CRR*, while dilative ε_v above 0.10% significantly decrease *CRR*. The *LRR* relationship for dilative ε_v from the single element simulations using the r_u=0.98 criteria indicates a larger reduction in *CRR* for a given ε_v compared to the simulation results using the γ=3% criteria, which is consistent with the behavior of the contractive ε_v results. The effect of dilative ε_v on *CRR* appears to be smaller than the effect of contractive ε_v on *CRR*; e.g., a contractive ε_v of 0.10% increases *CRR* by 45-50%, while a dilative ε_v of 0.10% decreases *CRR* by 15-36%.

ADJUSTMENT OF CENTRIFUGE DATA PAIRS FOR DRAINAGE EFFECTS

The results of the single element simulations using Approach 2 with the r_u=0.98 criteria are used to adjust the centrifuge *CRR*-q_{c1N} pairs for contractive or dilative volumetric strain. Figure 14

replots Figure 7 with the pairs adjusted for partial drainage effects. *CRR* and *CSR* values were increased 0 to 36% or decreased 0 to 63% depending on the amount of ε_v generated during shaking. *CRR*s for high, medium, and low confidence pairs were adjusted 4-38%, 0.9-26%, and 0-63%, for contractive ε_v, and 3-36%, 6%, and 0-28%, for dilative ε_v, respectively; *CSR*s for non-triggering pairs were adjusted 0-45% for contractive ε_v and 0-25% for dilative ε_v. If the simulation results of Approach 1 with the r_u=0.98 criteria were used instead to perform the adjustment, *CRR* and *CSR* values for pairs with contractive ε_v would decrease 0-63%. If the simulation results using the shear strain criteria to define CRR were used to perform the adjustment, *CRR* and *CSR* values for pairs with contractive ε_v would decrease 0-49% (Approach 1) and 0-27% (Approach 2), whereas *CRR* and *CSR* values for pairs with dilative ε_v would increase 0-15% (Approach 2). If the relation proposed by Okamura and Soga (2006) was used to perform the adjustment, *CRR* and *CSR* values for pairs with contractive ε_v would be decreased by 0-30%. The adjustments to the *CRR*s for partial drainage effects, regardless of which approach is used, improved the agreement of the centrifuge data with the case history based correlations for each of the four categories of data shown in Figures 14a-d, but the effects were not large and did not significantly change the variability in the centrifuge *CRR*-q_{c1N} data for these different data categories.

DISCUSSION

There are several differences between the partial saturation experimental studies and simulations, and the centrifuge model tests and single element simulations described in this study, which may influence *CRR*, pore pressure, and ε_v generation. *CRR* and pore pressure generation have been shown to be influenced by differences in fabric and sample preparation (e.g., Mullis et al. 1977, Abdoun et al. 2013). The experimental studies by Okamura and Soga (2006) and Yoshimi et al. (1989) were performed on wet tamped and air pluviated Toyoura sand, respectively, and prepared

to target D_R of 40 and 60%; the simulations by Zhang et al. (2016) were performed for Toyoura and Nevada sand prepared to target D_R of 30, 50, and 70%. Comparatively, the centrifuge models in this study were air pluviated Ottawa sand models prepared at D_{Ro} of 25, 43, and 80%, and subjected to multiple straining events to achieve a range of relative density. Additionally, while the analyses described in this study generate contractive volumetric strains ranging from 0 to 4%, the volumetric strains from the partial saturation database range from 0.3-7%. The comparison of volumetric strains due to partial drainage with volumetric strains in partially saturated samples is complicated by the influence of matric suction on the partially saturated samples. For example, pore water suction significantly affected seismic surface settlements of partially saturated sand models (degree of saturation ranging from 32 to 68%) in a series of dynamic centrifuge tests by Morteza and Ghayoomi (2017), with the observed effects reasonably attributed to the effects of suction on the sand properties and the subsequent dynamic response of the sand profile (e.g., Ghayoomi et al. 2013). The studies referenced herein provide reasonably consistent trends between *LRR* and the ε_v due to either partial drainage or compression of partially saturated sands for degrees of saturation greater than about 70%, but the effects of pore water suction can be expected to be greater for greater suction magnitudes (e.g., finer sands with smaller pore sizes) and smaller confining stresses.

The approach presented herein can inform the understanding of how centrifuge model and case history data may be influenced by partial drainage during cyclic loading. Centrifuge models studies using unscaled pore fluid viscosity have observed large effects due to partial drainage, with increases in *CRR* by up to a factor of 10. For other testing or field conditions, the magnitude of volumetric strains at the time of triggering and influence on *CRR* will depend on the properties of the: material (permeability, compressibility), loading (intensity, duration, frequency content), and

site geometry (stratigraphy, permeability contrast, continuity of strata). Estimation of the volumetric strain during shaking by the inverse analyses approach presented or guided by measurements of surface settlement may provide an indication of the influence of partial drainage on *CRR*.

CONCLUSION

The effects of partial drainage on the *CRR*s and *CRR*-q_{c1N} data pairs for saturated sand in a set of dynamic centrifuge models studies was evaluated using a combination of inverse analyses of dense PPT arrays to determine volumetric strains, single element numerical simulations to investigate how dilative or contractive volumetric strains can affect the *CRR*, and comparisons of the simulation results with experimental and simulation data by others. Non-uniform volumetric strains developed throughout the soil profiles during and after shaking. Volumetric strains during shaking were usually smaller than those during post-shaking dissipation. Surface settlements obtained by numerical integration of the volumetric strain profiles were in reasonable agreement with measured settlement values. The reasonable agreement between measured and computed settlements supports the described method for calculating profiles of gradient and volumetric strain. Examination of volumetric strains with other features of dynamic response provide insight into the role of volumetric strain on liquefaction triggering on a system-level basis. Single element simulations for the effectiveness of contractive volumetric strains show reasonable agreement with previous laboratory and numerical studies. The developed relationships for *LRR* versus volumetric strain were used to adjust centrifuge *CRR*-q_{c1N} pairs to equivalent perfectly-undrained conditions. Triggering points moved 0-63% while non-triggering points moved 0-45%. The adjustments to

the *CRR*s for partial drainage effects made the centrifuge data agree slightly better with the case history based correlations, but the effects were not large.

ACKNOWLEDGEMENTS

This material is based upon work supported by the National Science Foundation (NSF) under grants CMMI-1300518 and CMMI-1635398. Operation of the centrifuge facility at the University of California at Davis was supported as part of the Natural Hazards and Engineering Research Infrastructure (NHERI) network under NSF award CMMI- 1520581. Any opinions, findings, and conclusions or recommendations expressed in this material are those of the authors and do not necessarily reflect the views of the National Science Foundation. The authors appreciate the assistance of the staff of the Center for Geotechnical Modeling at UC Davis.

REFERENCES

Abdoun, T., Gonzalez, M. A., Thevanayagam, S., and Dobry, R. (2013). "Centrifuge and large-scale modeling of seismic pore pressures in sands: Cyclic strain interpretation". *Journal of Geotechnical and Geoenvironmental Engineering*. 10.1061/(ASCE)GT. 1943-5606.0000821, 1215-1234.

Alarcon-Guzman, A., Chameau, J. L, Leonards, G. A., Frost, J. D. (1989). "Shear modulus and cyclic strength behavior of sands". *Soils and Foundations*, 29(4), 105-119.

Arulanandan K., Sybico J. Jr., (1992). "Post-liquefaction settlement of sand". Proceedings, Wroth Memorial Symposium, Oxford University, England.

Balakrishnan, A. (2000). "Liquefaction remediation at a bridge site". PhD. Dissertation, University of California, Davis.

Boulanger, R. W., and Idriss, I. M. (2015). "CPT-based liquefaction triggering procedure." J. of Geotechnical and Geoenvironmental Engineering, ASCE, 142(2): 04015065, 10.1061/(ASCE)GT.1943-5606.0001388.

Boulanger, R. W., and Ziotopoulou, K. (2017). "PM4Sand (Version 3.1): A sand plasticity model for earthquake engineering applications." Report No. UCD/CGM-17/01, Center for Geotechnical Modeling, Department of Civil and Environmental Engineering, University of California, Davis, CA, 113 pp.

Boulanger, R. W., Khosravi, M., Khosravi, A., Wilson, D. W. (2017). "Remediation of liquefaction effects for an embankment using soil-cement walls: Centrifuge and numerical modeling". Proc., Performance-based Design in Earthquake Geotechnical Engineering, PBD-III Vancouver, M. Taiebat et al., eds., ISSMGE Technical Committee TC203, paper 537.

Darby, K. M., Boulanger, R. W., DeJong, J.T. (2018a). "Volumetric strains from inverse analysis of pore pressure transducer arrays in centrifuge models". Proc., Geotechnical Earthquake Engineering and Soil Dynamics V, Geotechnical Special Publication 290, S. J. Brandenberg and M. T. Manzari, eds., ASCE, 626-636.

Darby, K. M., Boulanger, R. W., DeJong, J. T., and Bronner, J. D. (2018b). "Progressive changes in liquefaction and cone penetration resistance across multiple shaking events in centrifuge tests". *Journal of Geotechnical and Geoenvironmental Engineering*, ASCE, [In press].

Darby, K. M., Boulanger, R. W., and DeJong, J. T. (2017). "Effect of multiple shaking events on cone penetration resistances in saturated sand." Proc., Performance-based Design in Earthquake Geotechnical Engineering, PBD-III Vancouver, M. Taiebat et al., eds., ISSMGE Technical Committee TC203, paper 534.

Darby, K. M., Bronner, J. D., Parra Bastidas, A. M., Boulanger, R. W., and DeJong, J. T. (2016). "Effect of shaking history on cone penetration resistance and cyclic strength of saturated sand." Proceedings, Geotechnical and Structural Engineering Congress, Phoenix, AZ, Feb. 14-17, ASCE, 1460-1471.

Ghayoomi, M., McCartney, J. S., and Ko, H-Y. (2013). "Empirical methodology to estimate seismically induced settlement of partially saturated sand." *Journal of Geotechnical and Geoenvironmental Engineering*, 10.1061/(ASCE)GT.1943-5606.0000774.

Howell, R., Rathje, E. M., Kamai, R., and Boulanger, R. W. (2012). "Centrifuge modeling of prefabricated vertical drains for liquefaction remediation." *Journal of Geotechnical and Geoenvironmental Engineering*, ASCE, 138(3), 262-271.

Itasca (2016). FLAC, Fast Lagrangian Analysis of Continua, User's Guide, Version 8.0. Itasca Consulting Group, Inc., Minneapolis, MN.

Jafarzadeh, F. and Yanagisawa, E. (1995). "Settlement of sand models under unidirectional shaking". 1st International Conference on Earthquake Geotechnical Engineering, K. Ishihara, ed., IS-Tokyo, 693-698.

Kamai, R., and Boulanger, R. W. (2010). "Characterizing localization processes during liquefaction using inverse analyses of instrumentation arrays." Meso-Scale Shear Physics in Earthquake and Landslide Mechanics, Y. H. Hatzor, J. Sulem, and I. Vardoulakis, eds., CRC Press, 219-238.

Kamai, R., and Boulanger, R. W. (2012). "Single-element simulations of partial-drainage effects under monotonic and cyclic loading." *Soil Dynamics and Earthquake Engineering*, 35(29-40).

Kokusho, T. (2003). “Current state of research on flow failure considering void redistribution in liquefied deposits”. *Soil Dynamics and Earthquake Engineering*, 23 (7), 585-603, 10.1016/S0267-7261(03)00067-8.

Kulasingam, R., Malvick, E. J., Boulanger, R. W., and Kutter, B. L. (2004). “Strength loss and localization at silt interlayers in slopes of liquefied sand.” *Journal of Geotechnical and Geoenvironmental Engineering,* 10.1061/(ASCE)1090-0241(2004)130:11(1192).

Kutter, B. L., Chou, J.-C., and Travasarou, T. (2008). "Centrifuge testing of the seismic performance of a submerged cut-and-cover tunnel in liquefiable soil." *Geotechnical Earthquake Engineering and Soil Dynamics IV*, GSP 181, ASCE.

Malvick, E. J., Kutter, B. L., Boulanger, R. W., and Kulasingam, R. (2006). “Shear localization due to liquefaction-induced void redistribution in a layered infinite slope.” *Journal of Geotechnical and Geoenvironmental Engineering,* 10.1061/(ASCE)1090-0241(2006)132:10(1293).

Malvick, E. J., Kutter, B. L., Boulanger, R. W. (2008). “Postshaking shear strain localization in a centrifuge model of a saturated sand slope”. *Journal of Geotechnical and Geoenvironmental Engineering*, ASCE 132(2), 164-174.

Morteza, M. and Ghayoomi, M. (2017). “Centrifuge tests to assess seismic site response of partially saturated sand layers”. *Soil Dynamics and Earthquake Engineering*, 94(254-265), 10.1016/j.soildyn.2017.01.024.

Mulilis, J. P., Seed, H. B., Chan, C. K., Mitchell, J. K., and Arulanandan, K., 1977. Effect of sample preparation on sand liquefaction, *Journal of Geotechnical Engineering Division*, ASCE 103(GT2), 91–108.

National Research Council (NRC) (1985). Liquefaction of Soils During Earthquakes, National Academy Press, Washington, DC, 240 pp.

Okamura, M. and Soga, Y. (2006). "Effects of pore fluid compressibility on liquefaction resistance of partially saturated sand". *Soils and Foundations*, JGS 46(5), 695-700.

Okamura, M., Nelson, F., and Watanabe, S. (2018). "Effect of pre-shaking on liquefaction resistance of sands with different initial fabrics". *Soil Dynamics and Earthquake Engineering [In press]*.

Parra Bastidas, A. M., Boulanger, R. W., Carey, T. J., DeJong, J. T. (2016). "*Ottawa F-65 sand data from Ana Maria Parra Bastidas"*, NEEShub, http://dx.doi.org/10.17603/DS2MW2R.

Seed, H. B., Idriss, I. M., Makdisi, F., Banerjee, N. (1975). *Representation of irregular stress time histories by equivalent uniform stress series in liquefaction analyses,* Report No. EERC 75-29, Earthquake Engineering Research Center, University of California at Berkeley, CA, October.

Taiebat, M., Shahir, H., and Pak, A. (2007). "Study of pore pressure variation during liquefaction using two constitutive models for sand". *Soil Dynamics and Earthquake Engineering*, 27(1), 60-72.

Whitman, R. V. (1985). "On liquefaction." *Proc., 11th Int. Conf. on Soil Mechanics and Foundation Engineering,* Balkema, Rotterdam, Netherlands, 1923-1926.

Yoshimi, Y., Tanaka, K., Tokimatsu, K. (1989). "Liquefaction resistance of a partially saturated sand". *Soils and Foundations*, JGS 29(3), 157-162.

Zhang, B., Muraleetharan, K. K., Liu, C. (2016). "Liquefaction of unsaturated sands". *International Journal of Geomechanics*, 10.1061/(ASCE)GM.1943-5622.0000605, D4015002.

Ziotopoulou, K., and Boulanger, R. W. (2016). "Plasticity modeling of liquefaction effects under sloping ground and irregular cyclic loading conditions." Soil Dynamics and Earthquake Engineering, 84 (2016), 269-283, 10.1016/j.soildyn.2016.02.013.

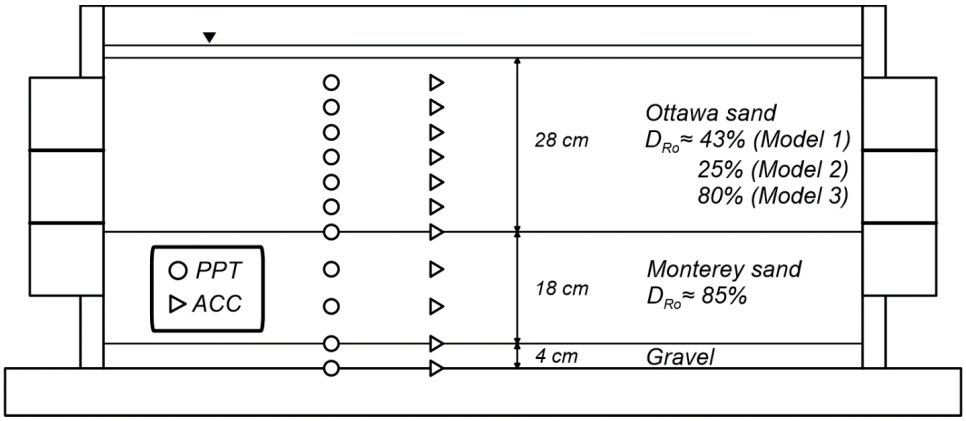

Figure 1. Centrifuge model cross section (dimensions in model scale).

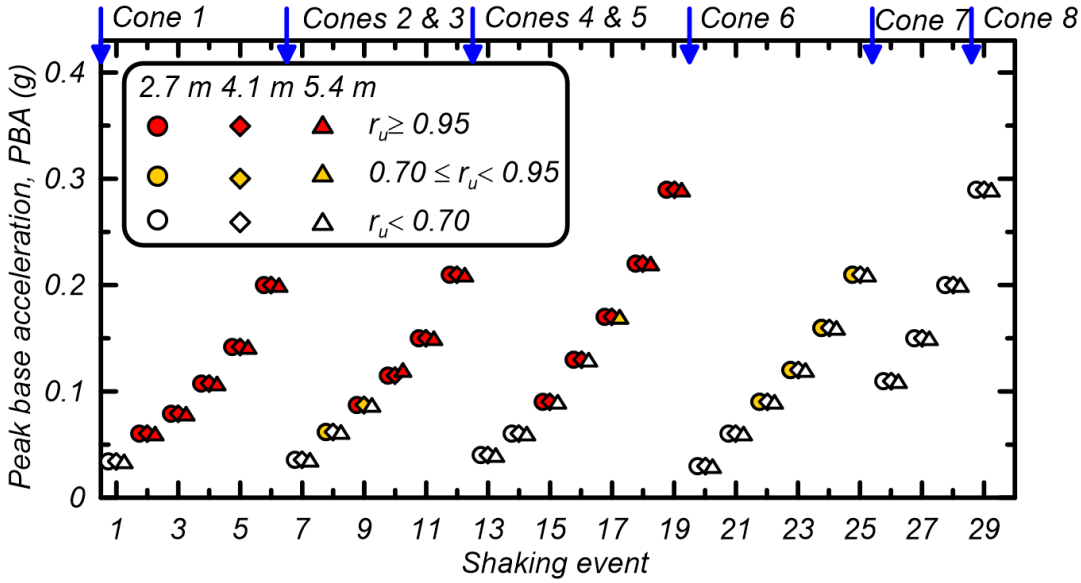

Figure 2. Time-line for Model 1 showing peak base acceleration, peak pore pressure ratios, and timing of cone penetration tests versus shaking event number.

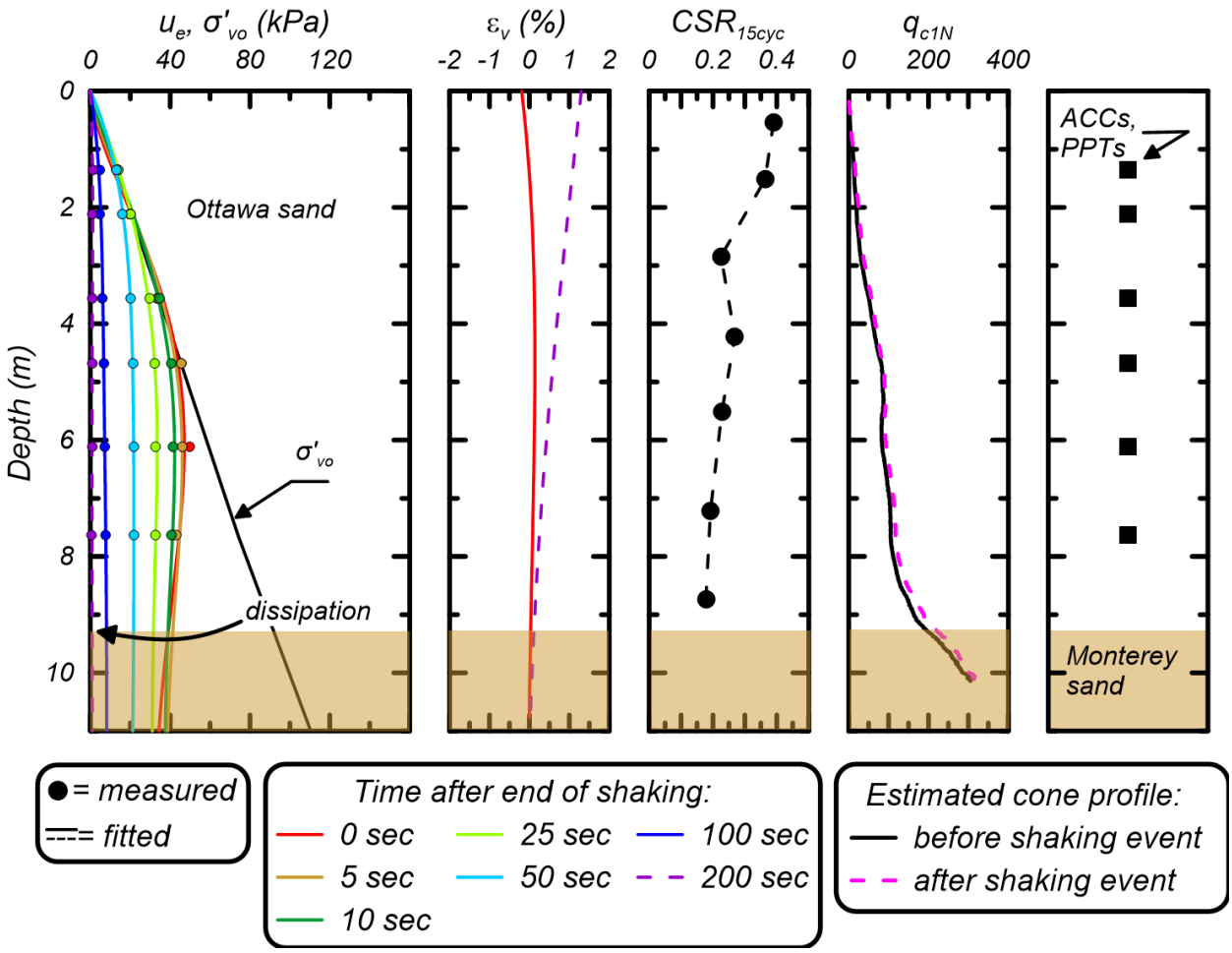

Figure 3. Isochrones of excess pore pressure and volumetric strain with the corresponding profiles for induced cyclic stress ratio and cone penetration resistance for the tenth shaking event (PBA = 0.12*g*) in Model 1 (D_{Ro} = 43%).

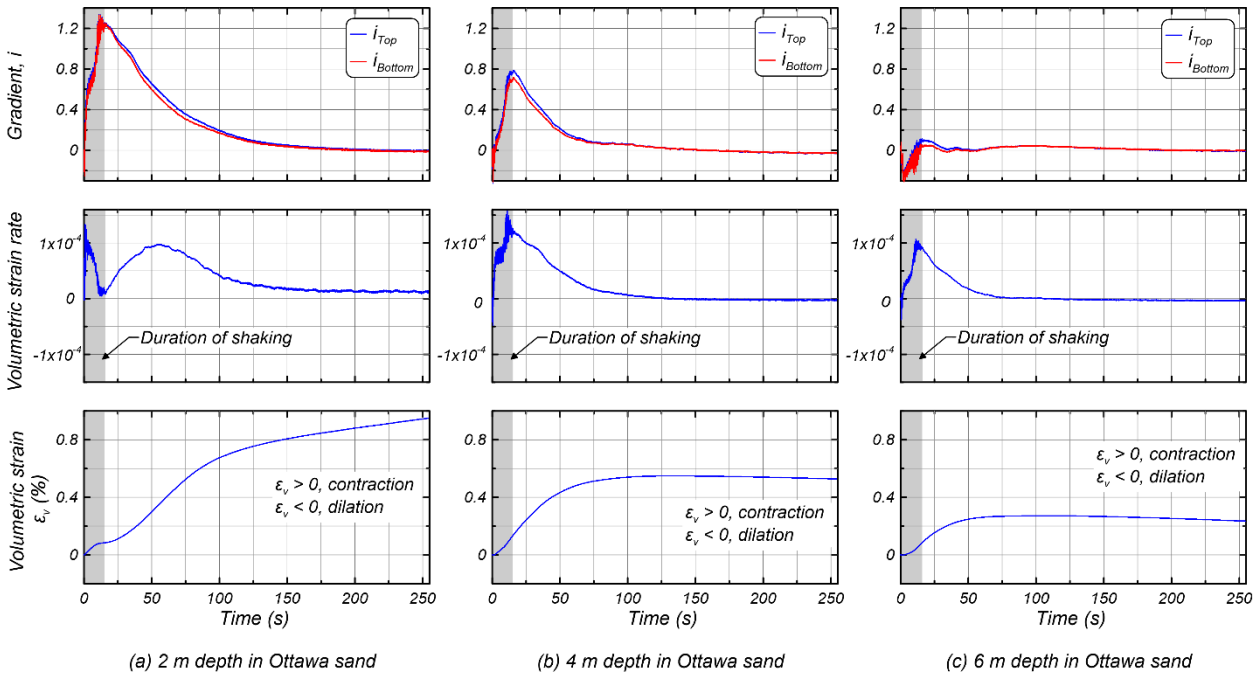

Figure 4. Time histories of hydraulic gradient, volumetric strain rate, and volumetric strain for the tenth shaking event in Model 1 at depths of (a) 2 m, (b) 4 m, and (c) 6 m.

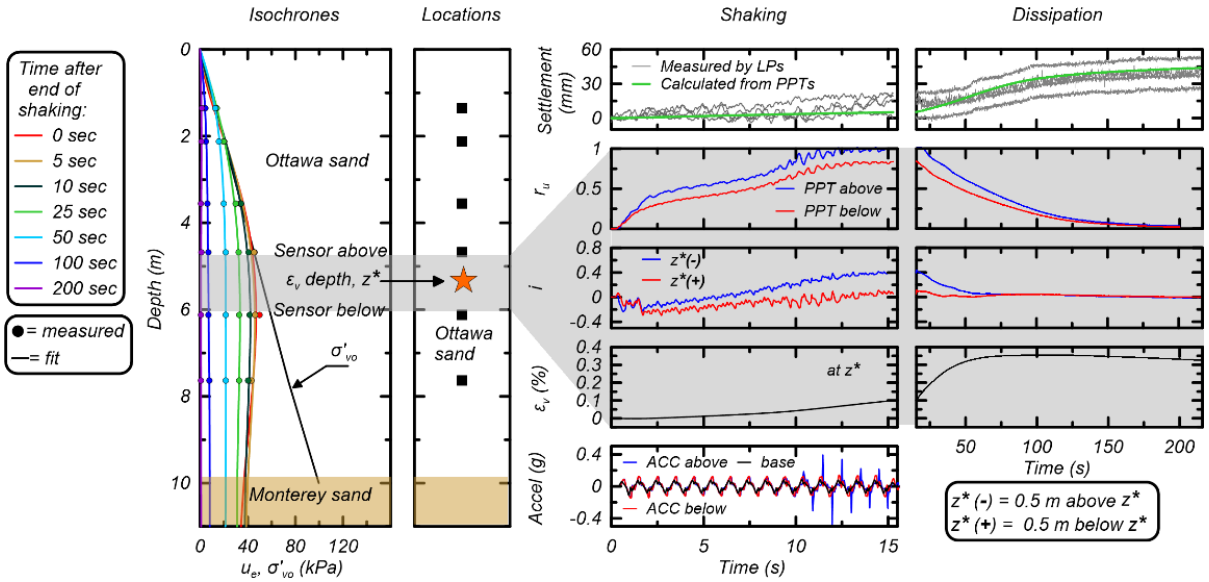

Figure 5. Response measures near the middle of the Ottawa sand layer during and after strong shaking for the tenth shaking event in Model 1.

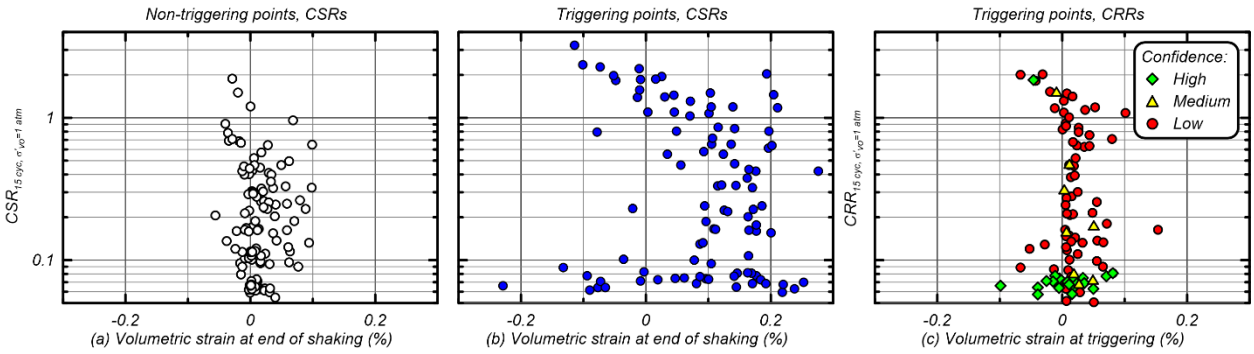

Figure 6. Relation between *CSR* and volumetric strain: (a) non-triggering points at the end of shaking, (b) triggering points at the end of shaking, and (c) triggering points up to the time of triggering.

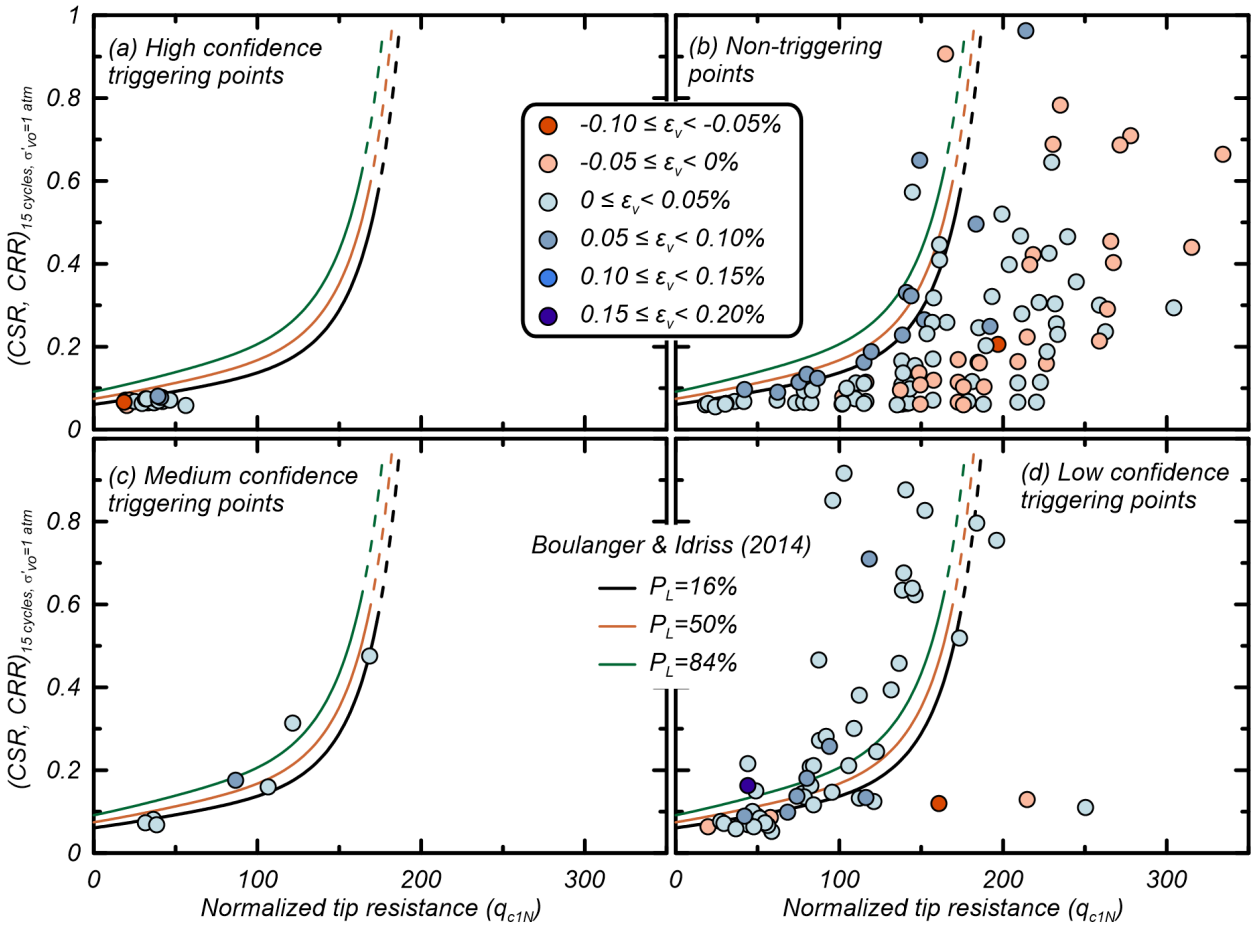

Figure 7. Volumetric strain for centrifuge *CRR-q_{c1N}* pairs: (a) high confidence triggering points, (b) non-triggering points, (c) medium confidence triggering points, and (d) low confidence triggering points.

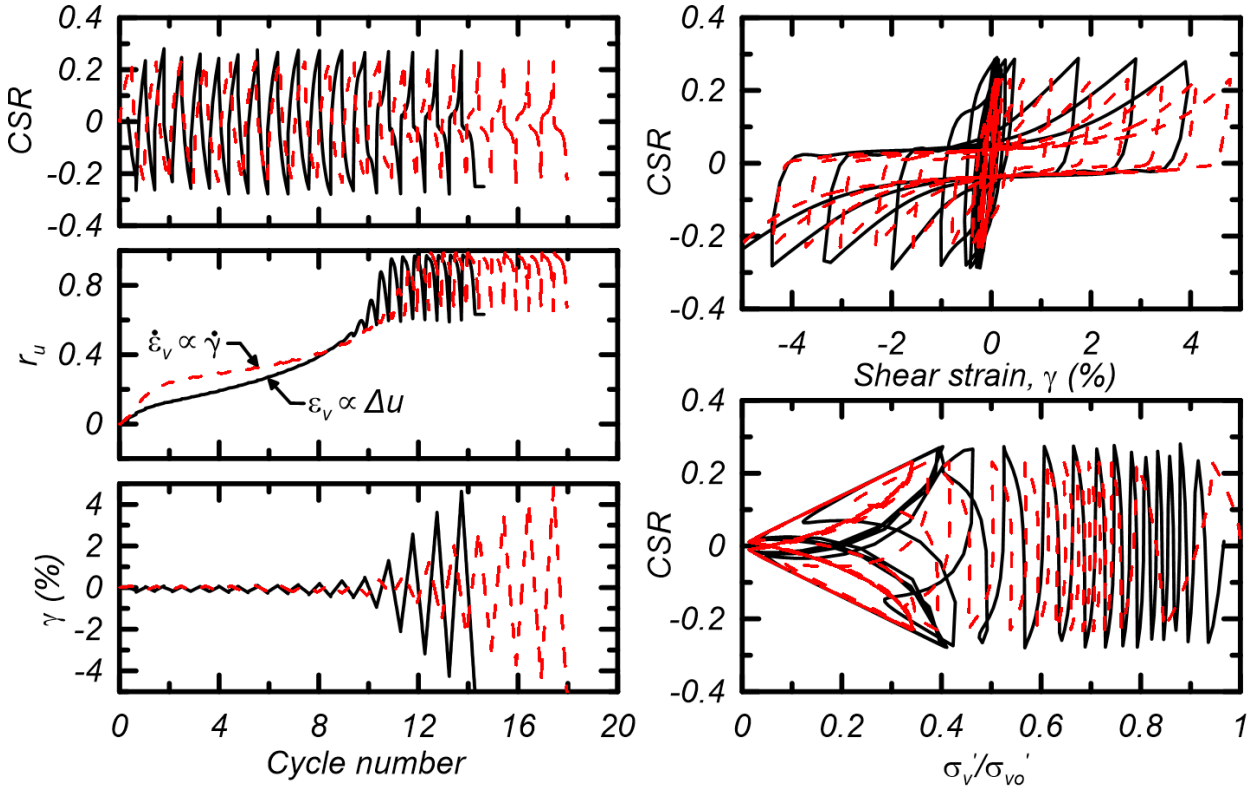

Figure 8. Comparison of simulation approaches to produce a volumetric strain of approximately 0.10% in 15 cycles.

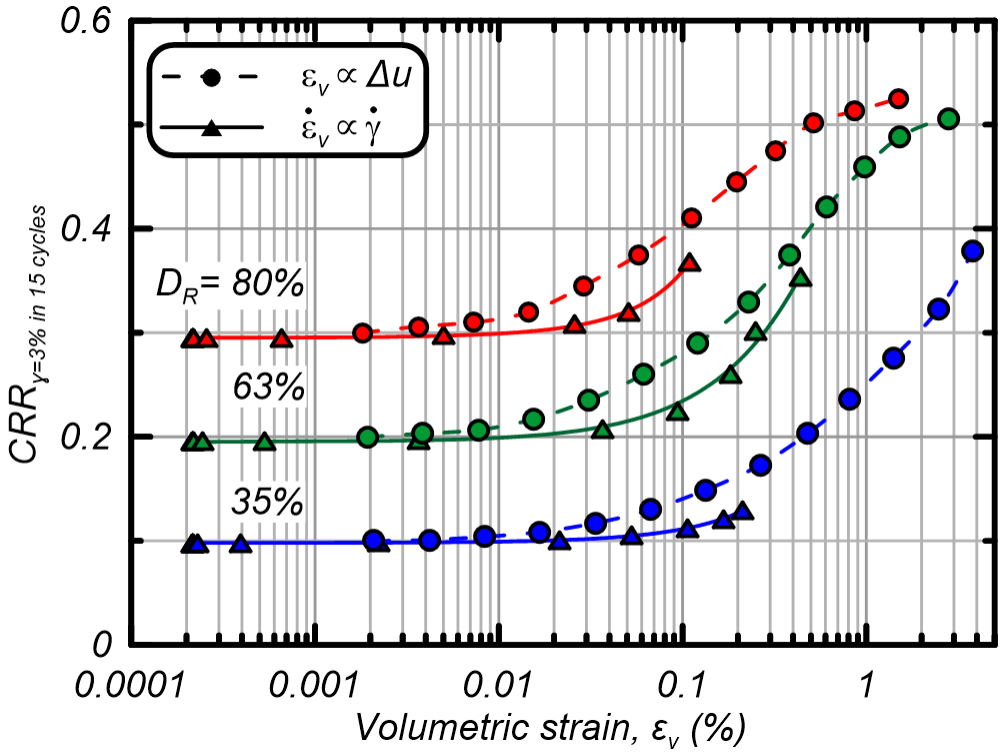

Figure 9. Comparison of *CRR* versus volumetric strain relationships from two simulation approaches at D_R=35, 63, and 80%.

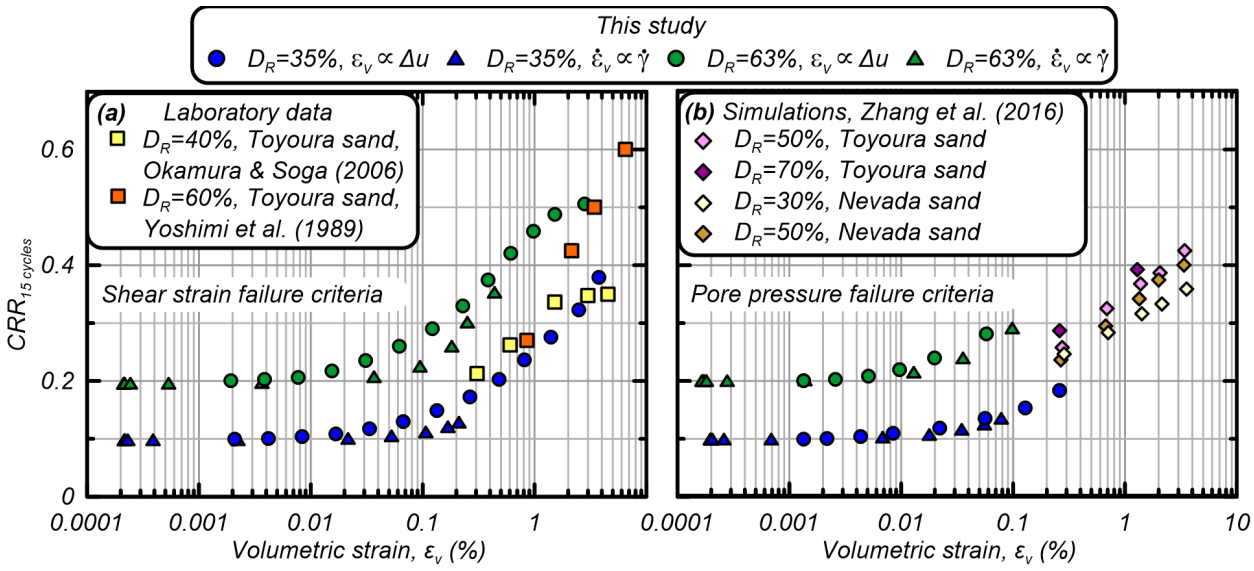

Figure 10. Comparison of simulated *CRR* versus contractive volumetric strain relationship with (a) laboratory data by others, and (b) simulations by others. All data for approximately 1.0 atm confining stress.

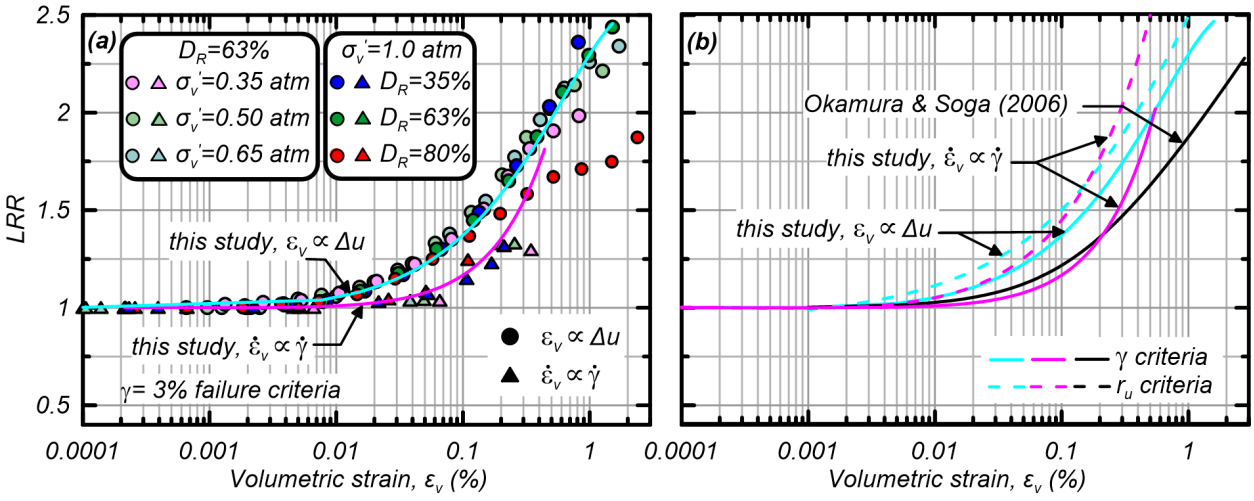

Figure 11. Relationship between *LRR* and contractive volumetric strain: (a) simulations for a range of densities and confining stresses using a 3% shear strain criteria, and (b) comparison of both criteria with recommendations of Okamura and Soga (2006).

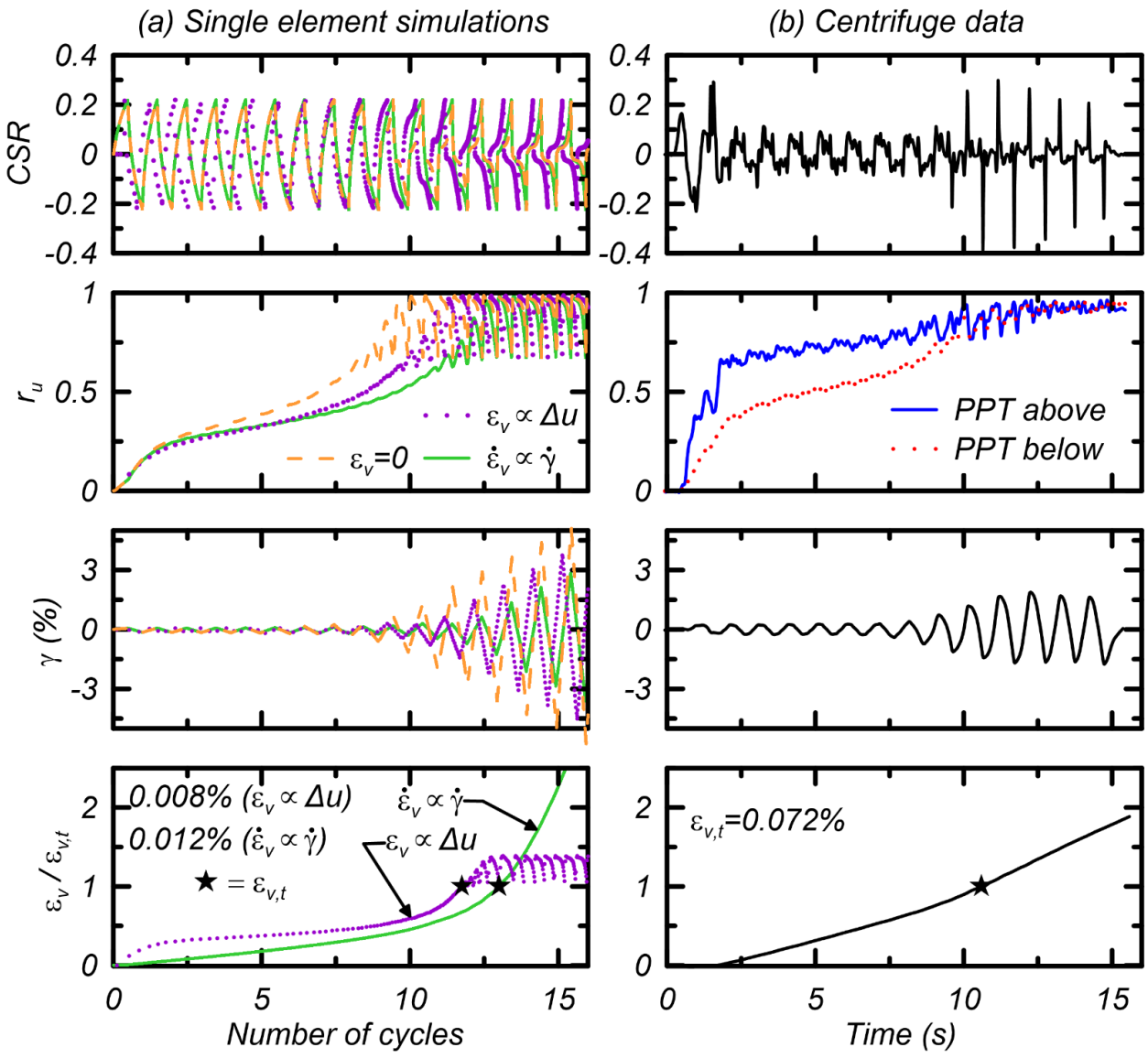

Figure 12. Comparison of stress, excess pore pressure, shear strain, and normalized volumetric strain in: (a) simulations with a uniform *CSR* of 0.22, and (b) centrifuge model with irregular *CSR* with early peak *CSR*s close to 0.22.

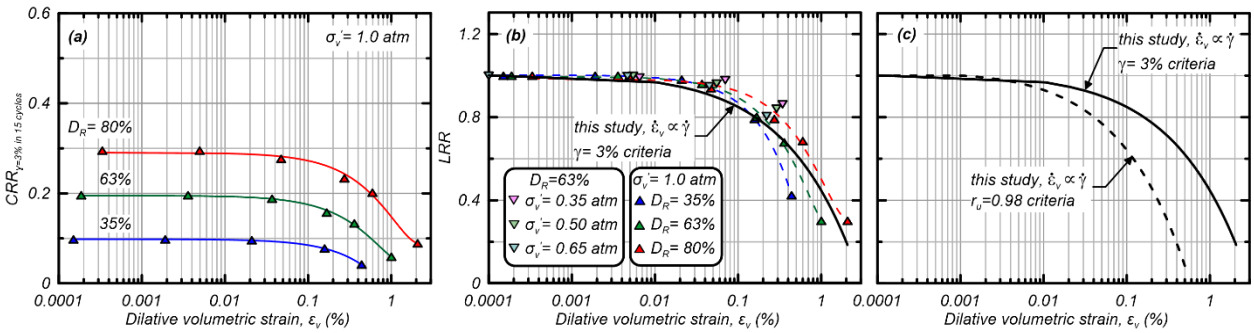

Figure 13. Effect of dilative volumetric strain on (a) *CRR* and (b) *LRR* from simulations, and (c) comparison of the dilative volumetric strain-*LRR* relationship for the two failure criteria.

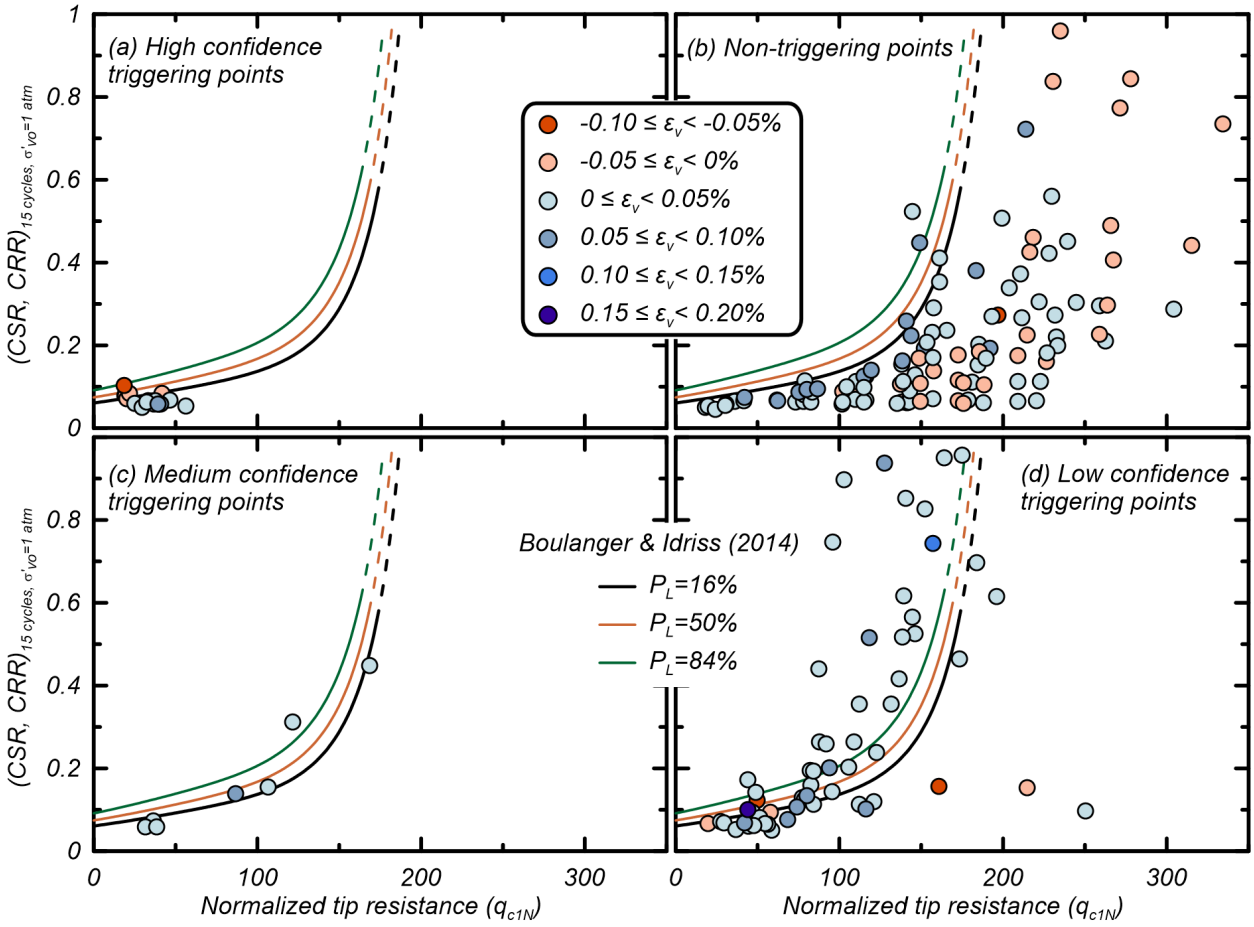

Figure 14. Centrifuge *CRR*-q_{c1N} pairs after adjustment to account for drainage effects: (a) high confidence triggering points, (b) non-triggering points, (c) medium confidence triggering points, and (d) low confidence triggering points.